MATERIALS SCIENCE

Multistep skyrmion phase transition driven by light-induced uniaxial strain

Bei Ding[1,2]†, Yadong Wang[1,3]†, Jiahui Meng[1]†, Xuejin Wan[4]†, Qingping Wang[5], Xinxing Xu[1], Yu Zhu[1], Minghui Qin[1], Xingsen Gao[1], Xiaoyan Zhong[6], Furong Chen[6], Jiawen Chen[1]*, Yangfan Hu[4]*, Xuewen Fu[7]*, Zhipeng Hou[1,2]*, Junming Liu[1,8]

Strain engineering in skyrmion-hosting multilayers holds promising potential for spintronic devices. However, conventional strain is below 0.5%, limiting exploration of unique properties under substantial strain. In addition, while uniaxial strain modifies magnetic interactions anisotropically, its influence on skyrmions is underexplored. Here, we integrate skyrmion-hosting multilayers with a flexible liquid crystal film, enabling multistep skyrmion phase transitions through light-induced uniaxial strain up to 1%. Our results demonstrate that skyrmion transitions are sensitive to strain magnitude and orientation. Strain below 0.6% parallel to stripes transforms them into skyrmions. Above 0.6%, skyrmions elongate perpendicularly to the strain direction, exhibiting a negative Poisson effect, with deformation up to 40% at 0.8% strain. Further strain reverts skyrmions back into stripes. Micromagnetic simulations reveal that these phenomena stem from strain-induced anisotropic modulation of Dzyaloshinskii-Moriya interaction. This approach, which combines flexibility, light activation, and substantial uniaxial strain, offers a promising strategy for low-power, multistate spintronic devices.

INTRODUCTION

Magnetic skyrmions are nanometric swirling spin configurations stabilized by a delicate interplay of magnetic anisotropy and Dzyaloshinskii-Moriya interaction (DMI) (1–12). Particularly in asymmetric heavy metal/ferromagnet multilayered films featuring interface DMI, these magnetic structures can be stabilized at room temperature, offering promising potential for advancing state-of-the-art spintronic devices (13–21). For practical applications, effective manipulation of skyrmions within multilayered films is crucial. Traditionally, this has primarily relied on spin-polarized current stimuli (1–6), which typically require high current density, leading to notable Joule heating. As an alternative, strain engineering can effectively avoid these issues as it involves no electric current. What adds further intrigue is their exotic magnetoelastic responses (22–39), including improved thermal stability (32, 35, 39), controllable multistate switching (22–24), and remarkable morphological flexibility (25, 28). These properties not only are of profound significance to fundamental physics but also greatly expand their functional potential, providing a transformative pathway for the future development of skyrmion-based technologies.

Despite its significance, effectively implementing strain strategies to manipulate skyrmions in multilayered films, which are crucial for practical device applications, remains constrained. The primary challenge is applying a sufficiently substantial strain on the skyrmion-hosting multilayers to overcome the energy barrier between the skyrmion phase and other magnetic configurations. Hitherto, the most common approach is to integrate the multilayer with a piezoelectric substrate subjected to an electrical field (17–19). However, the achievable strain typically falls below 0.5%, limiting the exploration of exotic topological magnetoelectrical properties that require substantial strain. In addition, previous studies have mostly focused on in-plane biaxial strain, which induces isotropic modifications to the DMI and magnetic anisotropy (18, 20, 21). In contrast, uniaxial strain allows for anisotropic modification, but its specific impact on the topological characteristics of skyrmions has not been thoroughly investigated. Thus, these limitations underscore the urgent need for developing a strain strategy that is capable of achieving substantial uniaxial strain variations in the skyrmion-hosting multilayers.

A promising and innovative approach is to use an azobenzene (AZO) liquid crystal film, which holds promising potential in flexible optoelectronics and display technologies (40). The AZO film consists of AZO mesogens that enable reversible photoisomerization. When exposed to ultraviolet (UV) light in the range of 340 to 380 nm, the AZO mesogens display a cis state with bent azo (—N≡N—) bonds (left panel of Fig. 1A). This bending induces a substantial in-plane uniaxial tensile strain on the outer curved surface of the liquid crystal film (right panel of Fig. 1A), which can be one order of magnitude larger than that in the piezoelectric substrate. Conversely, exposure to green light in the range of 420 to 550 nm transforms the cis state into a trans state with planar azo bonds (left panel of Fig. 1A), effectively relaxing the previously induced strain (right panel of Fig. 1B). This reversible photoisomerization feature allows for precise remote control of the uniaxial strain over a wide range by delicately adjusting the light wavelength and exposure time. Moreover, the strain can be maintained even after the light source is removed, making it highly suitable for constructing nonvolatile devices.

[1]Guangdong Provincial Key Laboratory of Optical Information Materials and Technology, Institute for Advanced Materials, South China Academy of Advanced Optoelectronics, South China Normal University, Guangzhou 510006, China. [2]Guangdong Provincial Key Laboratory of Quantum Engineering and Quantum Materials and Institute for Advanced Materials, South China Academy of Advanced Optoelectronics, South China Normal University, Guangzhou 510006, China. [3]Xi'an North Qinghua Electromechanical Co., Ltd., Xian 350300, China. [4]School of Materials Science and Engineering & Research Institute of Interdisciplinary Science, Dongguan University of Technology, Dongguan 523808, China. [5]College of Electronic Information and Automation, Aba Teachers University, Pixian Street, Wenchuan 623002 China. [6]Department of Materials Science and Engineering, City University of Hong Kong, Kowloon, China. [7]Ultrafast Electron Microscopy Laboratory, The MOE Key Laboratory of Weak-Light Nonlinear Photonics, School of Physics, Nankai University, Tianjin 300071, China. [8]Laboratory of Solid State Microstructures and Innovation Center of Advanced Microstructures, Nanjing University, Nanjing 211102, China.
*Corresponding author. Email: j.chen@m.scnu.edu.cn (J.C.); huyf@dgut.edu.cn (Y.H.); xwfu@nankai.edu.cn (X.F.); houzp@m.scnu.edu.cn (Z.H.)
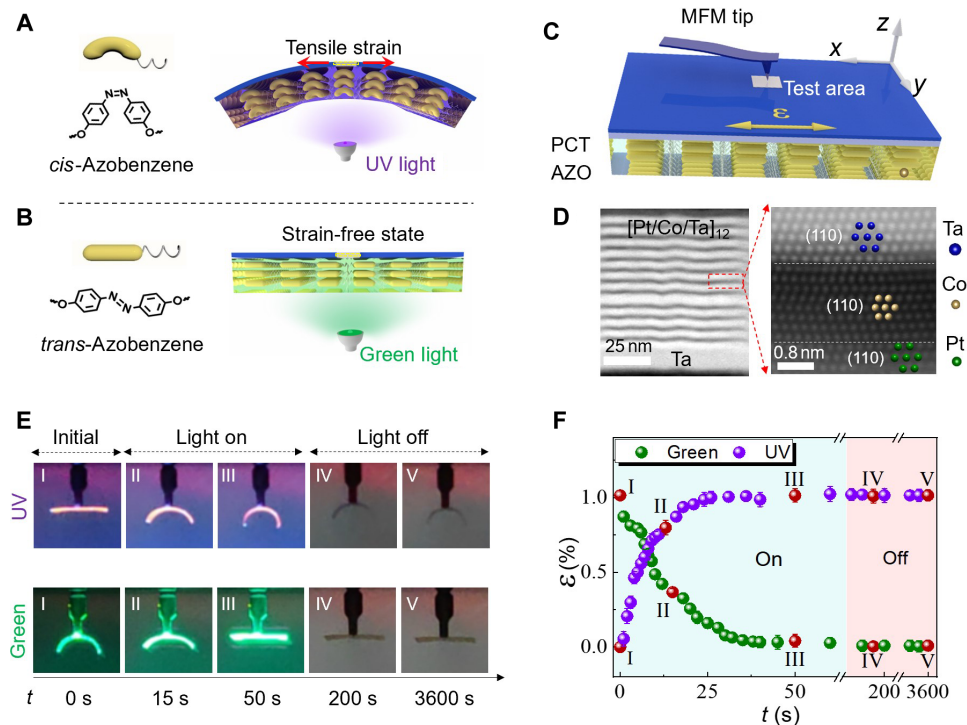†These authors contributed equally to this work.

Fig. 1. Fabrication of the [Pt/Co/Ta]₁₂/AZO heterostructure. Left panel of (**A**) showing the schematic diagram (upper) and molecular structure (lower) of the *cis*-azobenzene state. Right panel of (A) showing the schematic diagram of the [Pt/Co/Ta]$_{12}$/AZO heterostructure exposed to the UV light. A uniaxial in-plane tensile strain (red arrows) was generated at the curved surface of the heterostructure. Left panel of (**B**) showing the schematic diagram (upper) and molecular structure (lower) of the *trans*-azobenzene state. Right panel of (B) showing the schematic diagram of the strain-free [Pt/Co/Ta]$_{12}$/AZO heterostructure exposed to the green light. (**C**) Schematic diagram of the [Pt/Co/Ta]$_{12}$ (PCT)/AZO heterostructure in a rectangular coordinate system. The light-induced tensile strain (yellow arrow) orients along the *x* axis. Left panel of (**D**) showing the STEM image of the [Pt/Co/Ta]$_{12}$ cross section. The scale bar is 25 nm. Right panel of (D) showing the high-resolution STEM image of the [Pt/Co/Ta]$_{12}$ cross section. The inset shows the arrangement of Pt (green particle), Co (yellow particles), and Ta atoms (blue particles). Upper panel of (**E**) showing a sequence of optical photos (I → II → III) that capture the deformation dynamics of the heterostructure exposed to UV light at different exposure times (*t*). After removal of the UV light (IV → V), the deformation can be completely preserved. Lower panel of (E) showing a sequence of optical photos (I → II → III) that capture the deformation dynamics of the heterostructure exposed to green light at different *t*. After the removal of the green light (IV → V), the deformation can be completely preserved. (**F**) Relationship between the strain magnitude (*ε*) and the exposure time (*t*) for both green light (green dots) and UV light (purple dots). The red dots represent the strain magnitude corresponding to the optical photos displayed in (E).

In this study, we successfully combined the AZO liquid crystal film with [Pt/Co/Ta]$_{12}$ multilayers, which are known to host sub–100 nm room-temperature skyrmions (*41*), to explore controllable manipulation of skyrmions' topological characteristics through light-generated uniaxial tensile strain using in situ magnetic force microscopy (MFM). Our results demonstrate that skyrmion behavior is sensitive to both strain magnitude and orientation. When a small strain (<0.6%) is applied parallel to the stripe domains, they gradually transform into circular skyrmions (CSKs) as the tensile strain increases. However, once the strain exceeds the 0.6% threshold, these skyrmions elongate perpendicularly to the strain direction, demonstrating a negative Poisson effect (NPE) with a maximum morphology deformation amplified up to 40% at 0.8% strain. Further increasing the strain transforms the elongated skyrmions (ESKs) back into the stripe domains. Combining with micromagnetic simulations reveals that the multistep topological phase transition and negative Poisson effect of skyrmions are driven by strain-induced anisotropic modulation of DMI. Our work opens an exciting avenue for designing low-power, multistate flexible spintronic devices by leveraging the photostriction-magnetoelasticity coupling and anisotropic modulation of DMI in topological magnetic systems.

RESULTS

Fabrication of the [Pt/Co/Ta]₁₂/AZO heterostructure

We fabricated the [Pt/Co/Ta]$_{12}$/AZO heterostructure by depositing a [Pt (2.5 nm)/Co (2.2 nm)/Ta (1.9 nm)]$_{12}$/Ta (20 nm) multilayered stack onto a 50-μm-thick AZO liquid crystal film using the magnetron sputtering technique (Materials and Methods and Fig. 1C for details). During the sputtering process, the AZO film was affixed on a copper plate for efficient heat dissipation, preventing possible wrinkling because of overheating. Scanning transmission electron microscopy (STEM) analysis of the sample's cross section reveals that the as-prepared [Pt/Co/Ta]$_{12}$ magnetic multilayer has sharp and distinct interfaces (left panel of Fig. 1D). High-resolution STEM imaging further illustrated that the Pt (green particles), Co (yellow particles), and Ta (blue particles) atoms orderly arranged into the parallelogram lattice (the majority of the film exhibits an amorphous structure; fig. S1). Indexing their possible crystal structure identified the parallelogram lattice as the (110) plane within the cubic structure of Pt and Ta (space group of $Fm\bar{3}m$) and the hexagonal lattice as the (110) plane within the hexagonal structure of Co (space group of $P6_3/mmc$; right panel of Fig. 1D).

We then investigated the photostriction effect of the heterostructure by exposing it to UV (the wavelength is 365 nm) and green (the

wavelength is 465 nm) light from the bottom of the AZO layer. The light-induced dynamic behaviors were recorded as movies at 25 frames per second. Figure 1E displays a sequence of optical photos extracted from these movies, illustrating the detailed the deformation dynamics over exposure time (t). It is clearly observed that UV light induced notable bending in the film, and the bending radius (r) increased gradually with increasing t, eventually reaching saturation at $t = 25$ s (the upper row of Fig. 1E). Even after UV light was removed, the bending remained stable, indicating a nonvolatile feature. Conversely, exposure to green light gradually relaxed this bending, returning the heterostructure to the strain-free state ($r \rightarrow \infty$) at $t = 40$ s (the bottom row of Fig. 1E). The longer recovery time for the green light is attributed to the weaker absorption of the AZO film (fig. S2).

The bending of the AZO film generates a uniaxial tensile strain on the outer curved surface of the heterostructure. Because the MFM measurement area is only 5 μm by 5 μm, we assume that the tensile strain orients along the in-plane direction within such a small region. The magnitude of the resulting in-plane tensile strain (ε) can be qualitatively calculated using the bending strain formula

$$\varepsilon = \frac{d}{2r} \tag{1}$$

where d is the thickness of the heterostructure. As shown in Fig. 1F, the strain can be finely tuned up to a peak value of 1% by delicately adjusting the exposure time, providing an important basis for subsequent skyrmion manipulation.

Controllable creation and manipulation of skyrmions through light-induced uniaxial strain

We studied the strain effect on the magnetic domain evolution process using a homemade in situ light-induced strain setup integrated into the MFM, as shown in Fig. 2A. In this setup, light was injected from the bottom right of the heterostructure, which was draped on a quartz rod (Fig. 2B). Because of the gravity of the heterostructure, the measurement area can stay in close contact with the curved surface of the quartz rod, effectively eliminating possible height variations of the measurement area caused by light-induced sample bending (fig. S3). Before MFM measurements, an in-plane magnetic field of 1 T was applied using the VFM3 magnetic field component to align initial magnetic domains along the x axis, as schematically illustrated in Fig. 2B. After aligning the domains, the in-plane magnetic field was removed, and an out-of-plane magnetic field ($\mu_0 H$) was applied to nucleate skyrmions.

The magnetization process of the magnetic domain structures was first studied at the strain-free state (the bottom row of Fig. 2C). At $\mu_0 H = 0$ Oe, an array of stripe domains aligned along the x axis was observed. As $\mu_0 H$ increased, the stripe domains gradually fractured into smaller fragments and transformed into skyrmions at a critical magnetic field ($\mu_0 H_c$) of 130 mT. Light-induced tensile strain was then applied along the x axis by exposing the heterostructure to the UV light for a specific duration. After reaching the desired strain state, the UV light was turned off, and the strain could be maintained owing to the nonvolatile photostriction effect of the AZO film. As shown in the middle two rows of Fig. 2C, we observed that the application of strain caused $\mu_0 H_c$ to decrease with increasing ε, reaching a minimum value of 80 mT at $\varepsilon = 0.6\%$. In contrast to skyrmions stabilized solely by the magnetic field ($\mu_0 H_c = 130$ mT), the necessary assisting magnetic field was much lower, indicating that tensile strain effectively shifts the skyrmion phase to a lower-energy state. However, when the strain was applied perpendicular to the stripe domains (along the y axis), there was no obvious decrease in $\mu_0 H_c$ over the entire ε range (fig. S4), implying that the strain-assisted
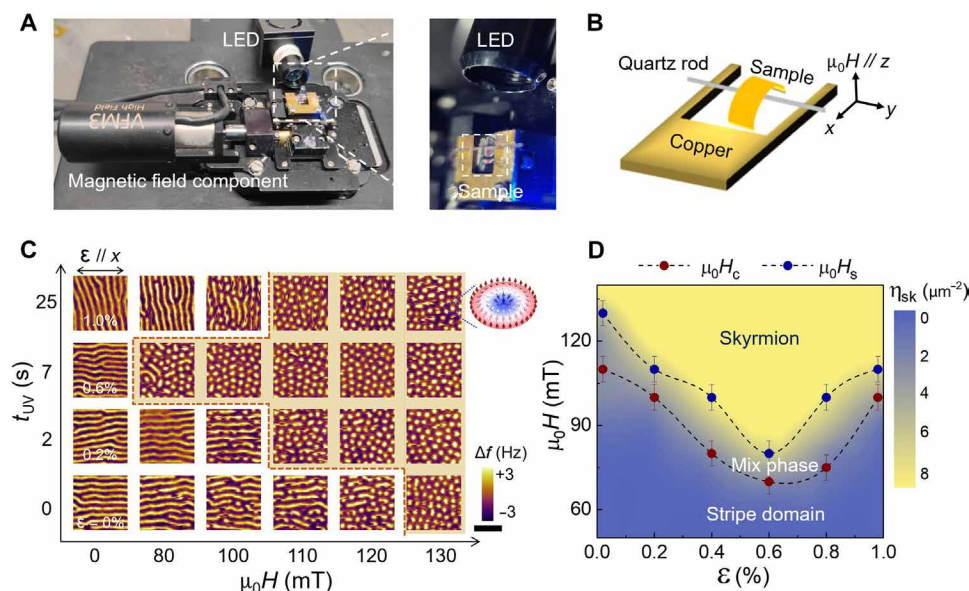

Fig. 2. Experimental setup for in situ light-induced strain MFM measurements. (**A**) Optical photograph of the homemade setup for in situ light-induced strain integrated into the MFM. The light was injected along the bottom right of the heterostructure, and the external magnetic field was applied using the VFM3 magnetic field component. Amplified optical photograph of the text area enclosed by the white dashed box in (A). LED, light-emitting diode. (**B**) Schematic illustration of the curved sample on the quartz rod, where external magnetic field $\mu_0 H$ was applied along the c direction. (**C**) Magnetic field–dependent MFM images measured under a fixed strain (ε): 0, 0.2, 0.6, and 1%. MFM tip resonant frequency shift (Δf) represents the image contrast. The scale bar in the MFM images is 1 μm. (**D**) Phase diagram of the [Pt/Co/Ta]$_{12}$/AZO heterostructure measured through fixed strain with varied magnetic field. Colors represent stripe domain, mixed phase, and skyrmion region. Different symbols indicate different phase boundaries. The blue dots represent the critical magnetic field for the transformation from mix phase to skyrmion ($\mu_0 H_s$).

skyrmion nucleation depends on the strain's orientation relative to the stripe domains.

We also found that, with increasing ε above 0.6%, the strain's assistance effect on skyrmion nucleation was suppressed, causing μ_0H_c to increase accordingly with increasing ε (top row of Fig. 2C). This suppression is likely due to strain-induced rotation of the stripe domains, which forces them to align perpendicularly to the strain direction. To better illustrate the magnetic field–dependent domain evolution process under strain, we plotted a color map based on more detailed MFM results (fig. S5), as shown in Fig. 2D. Here, the yellow and blue and their intermediate areas represent the skyrmion, stripe, and skyrmion-stripe mixing states, respectively. It is clearly demonstrated that a relatively small uniaxial tensile strain (ε ≤ 0.6%) promotes skyrmion nucleation, while a relatively large strain (ε > 0.6%) suppresses it. On the basis of these findings, we can conclude that both the strain magnitude and orientation play a crucial role in the manipulation of skyrmion phase transition.

We further explored strain's effect on domain evolution under a fixed out-of-plane magnetic field. Figure 3A and fig. S6 show a sequence of MFM images capturing the ε-dependent changes in magnetic domain at three typical magnetic fields. When μ_0H was below 80 mT (including 80 mT), only stripe domains were observed throughout the ε cycle, suggesting that the light-induced ε is insufficient to trigger a stripe-to-skyrmion transition under these magnetic field conditions. However, when the magnetic field increased to 95 mT, the stripe domains began to fracture as ε increased and ultimately transformed into circular skyrmions at ε = 0.6%, confirming the assisting effect of tensile strain on skyrmion nucleation. With ε increasing beyond 0.6%, the initially generated circular skyrmions were elongated along the y axis despite the strain aligning parallel to the x axis. This abnormal magnetoelectrical response can be identified as the negative Poisson effect of skyrmions, in contrast to the previously

reported positive Poisson effect (PPE) of skyrmions in the FeGe crystal (28). The occurrence of a negative or positive Poisson effect is proposed to stem from the competition between DMI and magnetic anisotropy in specific materials. A comprehensive analysis of the underlying physics will be presented in Discussion. The degree of skyrmion deformation can be quantitatively described by the ellipse oblateness defined by

$$f = 1 - \frac{b}{a} \qquad (2)$$

where a and b denote the ellipse axes perpendicular and parallel to the tensile strain, respectively (as schematically illustrated in the inset of Fig. 3A). Notably, at ε = 0.8%, f ranges from 20 to 40%, which is approximately two orders of magnitude larger than that of the lattice strain. Such substantial deformation suggests that skyrmion morphology could serve as an additional degree of freedom for skyrmion manipulation, providing a compelling route for the future exploration in areas, such as anisotropic magnetoelectrical properties (42, 43) and skyrmion-based multistate memories (44, 45). We attribute this morphology flexibility to the topological protection of skyrmions, which creates a high-energy barrier against transitioning to other domain structures. With ε further increasing up to 1%, strain transforms skyrmions into stripe domains. This observation suggests that the relatively larger tensile strain functions similarly to the decrease in the applied magnetic field, shifting the stripe phase to a lower-energy state.

Notably, from a topological perspective, the stripe domains observed in real materials often resemble deformed skyrmions. In this work, we classify deformed skyrmions with a length-to-width ratio greater than 3.0 as stripe domains, consistent with previous reports (4, 46–48).

When the heterostructure was exposed to the green light, ε decreased accordingly with increasing exposure time. A gradual transformation
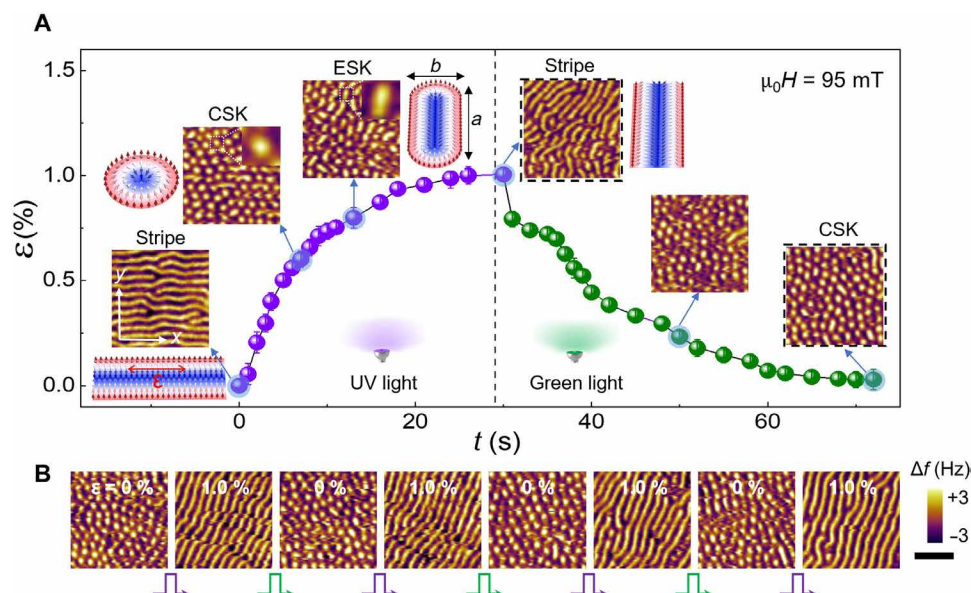

Fig. 3. Manipulation of skyrmions through the photostriction effect. (**A**) Relationship between the strain magnitude (ε) and the exposure time (t) for both UV light (purple dots) and green light (green dots). Insets showing the MFM images and corresponding schematic diagram at the dots enclosed by the red dashed boxes. A fixed magnetic field (μ_0H) of 95 mT was applied along the out-of-plane direction during the measuring process. The scale bar in the MFM images is 0.5 μm. CSK, circular skyrmion; ESK, elongated skyrmion. (**B**) Skyrmion-stripe binary switching achieved by exposing the heterostructure to UV light for 25 s (resulting in ε = 1%) and green light for 40 s (resulting in ε = 0%). MFM tip resonant frequency shift (Δf) represents the image contrast. The scale bar in the MFM images is 1 μm.

from stripe domains, back into elongated skyrmions, and then to circular skyrmions was observed. However, because of the topological protection, the circular skyrmion phase did not revert to the initial stripe domains upon strain release. We also found that the transformation of the skyrmions back into the stripe domain occurred at a narrow $\mu_0 H$ range. For instance, when $\mu_0 H$ increased to 100 mT, the skyrmions could not transform into the stripe domain anymore, even though elongated skyrmions appeared at $\varepsilon = 1\%$ (fig. S6). Furthermore, we have achieved the stripe-skyrmion reversal switching by exposing the heterostructure to UV light for 25 s (resulting in $\varepsilon = 1\%$) and green light for 40 s (resulting in $\varepsilon = 0\%$), as shown in Fig. 3B. This light-induced switching demonstrates promising potential for designing advanced flexible spintronic devices that use photostriction-magnetoelasticity coupling.

DISCUSSION

On the basis of the $[Pt/Co/Ta]_{12}/AZO$ heterostructure, we have achieved a strain-mediated light-induced multistep skyrmion phase transition. The next step involves a detailed exploration of the underlying physical mechanisms. It is widely recognized that the interplay between the effective magnetic anisotropy and the DMI plays a crucial role in the stabilization of skyrmions. Therefore, we will focus on examining how the light-induced uniaxial strain affects skyrmion phase transitions. While the saturation magnetization and Heisenberg exchange interaction are also important for the domain evolution, the strain achieved in our experiments is too small to notably affect them (Fig. 4A and fig. S7 for details).

First, we have calculated the strain-dependent effective magnetic anisotropy constant (K_{eff}) that determines the strength of magnetic anisotropy. To characterize the variation of magnetic anisotropy in the xy plane, we calculated two components: K_{eff}^{xz} and K_{eff}^{yz}, which correspond to the area difference between the out-of-plane magnetization curve and the magnetization curve measured along the x axis (K_{eff}^{xz}) and y axis (K_{eff}^{yz}), respectively (Fig. 4A and fig. S8 for details). Notably, directly measuring magnetization curves of a curved heterostructure may result in considerable deviation in K_{eff}. To address this issue, we deposited the $[Pt/Co/Ta]_{12}$ multilayer on a dented AZO film. After relaxing the AZO film, we obtained a flat heterostructure with specific tensile strain, enabling more precise magnetization measurements.

Figure 4B illustrates the established strain-dependent K_{eff}^{xz} and K_{eff}^{yz}. In the absence of strain, both constants exhibited negative values, implying in-plane magnetic anisotropy, meaning that the in-plane direction of the heterostructure is more easily magnetized than the out-of-plane direction. However, this does not imply that the magnetic easy axis (MEA) lies strictly within the xy plane. Instead, it forms a specific angle relative to the xy plane. We also observed that the values of K_{eff}^{xz} and K_{eff}^{yz} were nearly equal. This, combined with the angular orientation of MEA, suggests easy-cone magnetic anisotropy at the strain-free state, as schematically illustrated in Fig. 4C. As ε increased, both K_{eff}^{xz} and K_{eff}^{yz} increased accordingly, indicating a decrease in in-plane magnetic anisotropy (Fig. 4B), which suggests that the tensile strain induces a rotation of the MEA toward the z axis (as schematically illustrated in Fig. 4C). Moreover, the slope of the K_{eff}^{xz}-ε curve exceeds that of the K_{eff}^{yz}-ε curve, and the difference between K_{eff}^{xz} and K_{eff}^{yz} increases with enhancing ε. These results imply that the uniaxial tensile strain forces the in-plane component of the MEA to align along the y axis, that is, magnetic anisotropy transforms from the easy-cone type to an easy-axis type under the strain stimuli, as schematically illustrated in Fig. 4C.
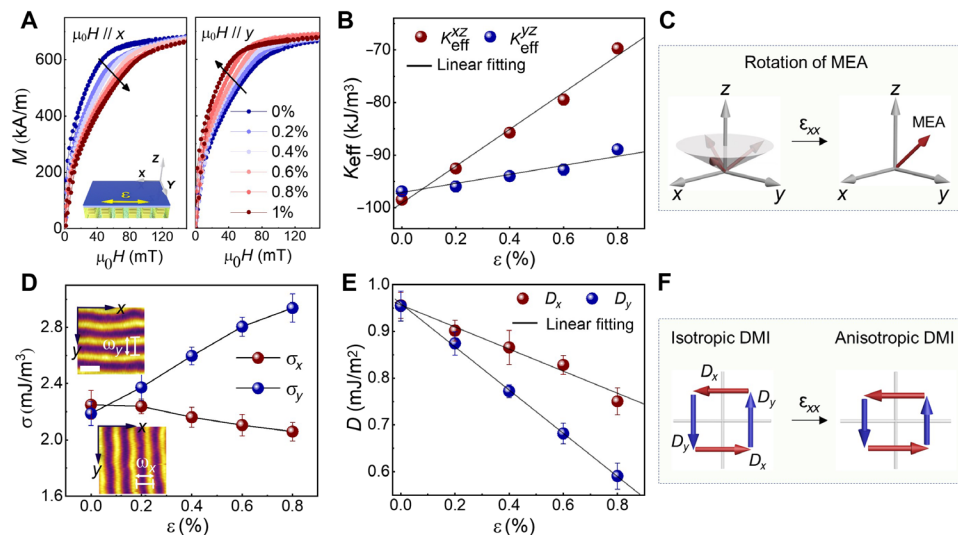

Fig. 4. Variation of magnetic anisotropy and DMI with light-induced strain. (**A**) Magnetization curves measured with the applied magnetic field along x (left panel) and y (right panel) axes at a strain range of 0 to 1%. The inset is the schematic diagram of the heterostructure in a rectangular coordinate system. (**B**) Variation of magnetic anisotropy in the xy plane with the light-induced strain along the x axis (ε_{xx}). K_{eff}^{xz} (red dots) and K_{eff}^{yz} (blue dots) correspond to the area difference between the out-of-plane magnetization curve and the magnetization curve measured along the x and y axes, respectively. The dependence of K_{eff}^{xz} or K_{eff}^{yz} with ε_{xx} is fitted using a linear law. (**C**) Schematic diagram for the rotation of MEA with the strain. (**D**) Strain-dependent domain wall energy along x (σ_x, red dots) and y (σ_y, blue dots) axes. Insets are MFM images measured at $H = 0$ mT. Domain periods along the x (ω_x) and y (ω_y) axes are schematically illustrated in the insets. The scale bar is 200 nm. (**E**) Variation of DMI constant along the x (D_x) and y (D_y) axes with ε_{xx}. The dependence of D_x or D_y with ε_{xx} is fitted using a linear law. (**F**) Schematic diagram for the transition from isotropic DMI at the strain-free state to the anisotropic DMI at the strain state.

Then, we studied the strain-induced variation of the effective DMI constant (D) that determines the strength of DMI. D was calculated using the domain wall energy (σ) formula (*19, 22, 23, 49*)

$$\sigma = 4\sqrt{AK_{\text{eff}}} - \pi |D| \tag{3}$$

where A is the exchange constant and is assumed to be a fixed constant ($A = 1.7 \times 10^{-11}$ J/m) over the whole strain range. σ can be calculated on the basis of the domain spacing model (*19, 22, 23, 50*)

$$\frac{\sigma}{\mu_0 M_s^2 h} = \frac{w^2}{h^2} \sum_{\text{odd } n=1}^{\infty} \left(\frac{1}{(\pi n)^3} \right) \left[1 - (1 - 2\pi nh/\omega)\exp(-2\pi nh/\omega) \right] \tag{4}$$

where h is the thickness of the film ($h = 72$ nm); ω is the low-field domain period; and M_s is saturation magnetization, which is fixed to be 750 kA/m at the both the strain-free and strained states. Combining these equations demonstrates that the anisotropic K_{eff} leads to an anisotropic distribution of D. Specifically, K_{eff}^{xz} and σ_x correspond to the DMI constant along the x axis (D_x), and the domain period extends along the x axis (Fig. 4D). Similarly, the DMI constant along the y axis (D_y) corresponds to K_{eff}^{yz} and σ_y, and the domain period extends along the y axis (Fig. 4D). Details about the establishment of σ_x and σ_y are presented in fig. S9. Using the magnetic parameters described above, we calculated D_x and D_y at different ε values (Fig. 4E). At $\varepsilon = 0$, the distribution of D is isotropic in the xy plane. When ε is applied along the x axis, both D_x and D_y decrease linearly. The slope of the ε-D_y curve (γ_y) is larger in absolute value than that of the ε-D_x curve (γ_x), resulting in an anisotropic distribution of D ($D_x \neq D_y$) in the xy plane, as schematically illustrated in Fig. 4F. This anisotropy reflects a differential response of the DMI to the uniaxial strain along different axes, which would notably affect the observed anisotropic skyrmion manipulation.

Using the experimentally established relationship between the strain, DMI, and magnetic anisotropy, we conducted micromagnetic simulations to further clarify their respective roles in the strain-mediated light-induced skyrmion phase transitions. Details about the simulations are described in Supplementary Note 1. We first set the simulated skyrmion phase at $\mu_0 H = 14$ mT as the initial state, and then a tensile strain was applied along the x axis to simulate its evolution process. The simulations reveal that, with increasing strain up to 1%, skyrmions elongated gradually along the y axis, reaching a maximum deformation of 50% at $\varepsilon = 0.4\%$; beyond $\varepsilon = 0.6\%$, the skyrmions transformed into stripe domains (fig. S10). Simultaneously, when $\mu_0 H$ was increased to 18 mT, the stripe domains were not formed anymore and only elongated skyrmions appeared at $\varepsilon = 1\%$. These results are well consistent with our experimental observations (Fig. 3A), validating our physical model. Hereafter, we analyzed the respective roles of DMI and magnetic anisotropy in the strain-induced skyrmion phase transition. Figure 5A displays the domain structures simulated on the basis of the strain-dependent K_{eff}^{xz} and K_{eff}^{yz} at $\mu_0 H = 14$ mT, with D_x and D_y fixed to be a constant at the strain-free state. The simulations show that applying strain along the x axis causes the skyrmions to elongate along the x axis, exhibiting a positive Poisson effect, contrary to the y axis elongation observed in experiments. In contrast, simulations considering only changes in D_x and D_y demonstrate a clear multistep magnetic phase transition from circular skyrmions to elongated skyrmions along y axis and then to stripe domains. This transition agrees well with the experimental results, suggesting that the observed topological phase transitions are primarily driven by changes in DMI rather than magnetic anisotropy.
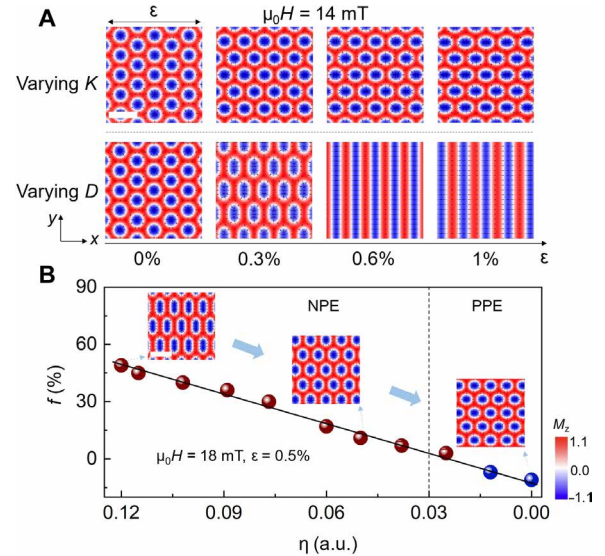

Fig. 5. Simulated magnetic domain evolution processes by varying *K* and *D*. The upper panel of (**A**) shows domain structures simulated on the basis of the ε-dependent K_{eff}^{xz} and K_{eff}^{yz} with D_x and D_y fixed to be their values at the strain-free state. ε is applied along the x axis direction with an out-of-plane magnetic field ($\mu_0 H$) of 14 mT. The lower panel of (A) shows domain structures simulated on the basis of the ε-dependent D_x and D_y with K_{eff}^{xz} and K_{eff}^{yz} fixed to be their values at the strain-free state. (**B**) Dependence of ellipse oblateness (*f*) on the degree of DMI anisotropy in the xy plane (defined by $\eta = 1 - D_x/D_y$) at $\mu_0 H = 18$ mT. A positive *f* represents the elongation of skyrmions along the y axis, corresponding to the negative Poisson effect (NPE) of skyrmions. Negative *f* represents the elongation of skyrmions along x-axis, corresponding to the positive Poisson effect (PPE) of skyrmions. The magnetization along the z axis (M_z) is represented by regions in red ($+M_z$) and blue ($-M_z$). The scale bars in [(A) and (B)] are 200 nm. a.u., arbitrary units.

We also observed that, when the slopes of the D-ε curve (both γ_x and γ_y) are fixed, variations in the initial D (i.e., D at the strain-free state) have little impact on the skyrmion deformation but substantially influence the skyrmion size (fig. S11). In contrast, decreasing DMI anisotropy in the xy plane (defined by $\eta = 1 - D_x/D_y$) results in a decrease in the skyrmion deformation (Fig. 5B and fig. S12). Notably, at $\eta = 0.02$, skyrmion deformation reaches zero, indicating no elongation. Further reduction in η causes the ellipse oblateness of skyrmion to fall below zero, showing that skyrmions elongate along the x axis, which corresponds to a positive Poisson effect. As established earlier, anisotropic manipulation of DMI induces a negative Poisson effect in skyrmions, while anisotropic changes in magnetic anisotropy result in a positive Poisson effect. Thus, we propose that the interplay between the DMI and magnetic anisotropy determines whether skyrmions exhibit a positive or negative Poisson effect of skyrmions in specific materials.

Last, we will discuss why the strain effect exhibits strong anisotropy. In fig. S13, we presented the calculated energy for three types of magnetic phase: (i) x-oriented stripe, (ii) y-oriented stripe, and (iii) deformed skyrmions, under varying ε_{xx} and a fixed out-of-plane magnetic field of 10 mT. For $\varepsilon = 0\%$, the two stripe configurations exhibit identical energy, indicating that the stripe orientation is isotropic without strain. As ε increases, the energy of both stripes increases linearly, with the y-oriented stripe maintaining the lower energy. This can be attributed to the x-oriented strain leading to a

lower DMI constant along the y axis (Fig. 5A). In this scenario, when the initial configuration consists of the x-oriented stripe, the strain tends to rotate it from the x axis to the y axis. However, in real materials, because of the pinning effect originating from factors such as magnetic hysteresis and/or defects, the expected stripe rotation cannot occur under relatively low strain. Only when the applied strain is strong enough to overcome the pinning effect, this rotation occurs, as experimentally observed in fig. S5. Furthermore, when ε increases above 0.15%, the energy of the skyrmion phase becomes lower than that of the stripe along the x axis. As a result, the x-oriented stripe transforms into the skyrmion phase under the strain stimuli. Because the y-oriented stripe maintains the lowest energy, the skyrmion phase remains stable as a metastable phase. As ε continues to increase above 0.3%, the skyrmion phase undergoes notable deformation, eventually losing stability. At this stage, the skyrmion phase disappears and transforms into the y-oriented stripe. In contrast, when the initial state consists of the y-oriented stripe, it remains as the ground state over the whole strain range, and thus, increasing the strain does not lead to skyrmion formation.

In conclusion, we have successfully fabricated the ferromagnetic film/liquid crystal flexible heterostructure and systematically explored the controllable manipulation of both the skyrmion's morphology and topological phase transition through the light-generated uniaxial tensile strain with a maximum value up to 1% using in situ MFM. We demonstrate that, as the strain increases up to the 0.6% threshold by delicately controlling the exposure time of UV light, circular skyrmions undergo elongation with a negative Poisson effect, reaching a maximum degree of deformation of up to 40%. A further increase in strain leads to the transformation of skyrmions back into stripe domains. Through theoretical analysis and calculations, we reveal that these exotic phenomena arise from the strain-induced anisotropic modulation of DMI. Our work uniquely combines the material flexibility and remote light activation with the skyrmion-based spintronic devices that are typically designed for magnetic memory and logic operations. This combination holds promising potential for the development of intelligent vision devices that seamlessly integrate light sensing, memory storage, and computational functions (*51*, *52*), thereby broadening the scope and potential applications of skyrmion-based technologies.

MATERIALS AND METHODS
AZO fabrication
The liquid-crystalline base composition mixture is synthesized by mixing (mol %) 4.15% of the AZO switch, 94.7% of liquid crystal monomers (C6M/C6BP/C6BPN in a molar ratio of 1.17:2.96:1), 0.04% of the chiral dopant (S-811), and 1.1% of the photoinitiator (Irgacure 819). The amount of chiral dopant S-811 was adjusted to induce a 50-μm quarter pitch. All components were brought together by dissolution in dichloromethane, and then the solvent was evaporated at 40°C. Afterward, the liquid crystal was heated up to the isotropic phase (60°C) for 3 min, injected into the liquid-crystal cell, left at 60°C for 1 hour, and then gradually cooled down to obtain the nematic phase (40°C) before photopolymerization with visible light for 40 min using an Edmund MI-150 high-intensity illuminator equipped with a cutoff filter ($\lambda \geq 420$ nm, 77 to 170 mW cm^{-2}). The polymerized film was retained in the cell at 40°C overnight for optimal polymerization. Polymerization was performed between two glass substrates separated by 10- to 50-μm-thick spacers. The glass substrates were coated

with poly(vinyl alcohol) and rubbed for promoting a twist geometry for the liquid crystal. After photopolymerization, the polymer film was separated from the substrates. Then, it was sliced into rectangular pieces of different sizes for the substrate of magnetic materials.

[Pt/Co/Ta]$_{12}$/AZO heterostructure fabrication
The [Pt (2.5 nm)/Co (2.2 nm)/Ta (1.9 nm)]$_{12}$/Ta (20 nm) multilayer was deposited on the AZO substrate by magnetron sputtering with a base pressure lower than 5×10^{-5} Pa and a working Ar pressure of 0.45 Pa. The Ta (20 nm) layer served as a buffer layer to provide a flat surface for growing a high-quality Pt/Co/Ta multilayer.

Magnetic force microscopy measurements
The MFM observations are performed with scanning probe microscopy (MFP-3D, Asylum Research). For the measurements, a low-moment magnetic tip (SSS-MFMR, Nanosensors) is selected, and the distance between the tip and the sample is maintained at a constant distance of 20 nm. Preceding the MFM measurements, a substantial in-plane magnetic field of 1 T was preapplied to align the initial magnetic domains along the direction of the magnetic field. Subsequently, the in-plane magnetic field was removed and an out-of-plane magnetic field ($\mu_0 H$) was applied to induce the nucleation of skyrmions. For the MFM measurements, a low-moment tip with a magnetic field magnitude of less than 100 Oe was used to minimize the influence of the tip's stray field on the magnetic domain structures.

Supplementary Materials
This PDF file includes:
Figs. S1 to S13
Supplementary Note 1
References

REFERENCES AND NOTES
1. Y. Tokura, N. Kanazawa, Magnetic skyrmion materials. *Chem. Rev.* **121**, 2857–2897 (2021).
2. A. Fert, N. Reyren, V. Cros, Magnetic skyrmions: Advances in physics and potential applications. *Nat. Rev. Mater.* **2**, 17031 (2017).
3. Y. Zhou, Magnetic skyrmions: Intriguing physics and new spintronic device concepts. *Natl. Sci. Rev.* **6**, 210–212 (2018).
4. R. Wiesendanger, Nanoscale magnetic skyrmions in metallic films and multilayers: A new twist for spintronics. *Nat. Rev. Mater.* **1**, 16044 (2016).
5. Y. D. Wang, Z. J. Wei, H. R. Tu, C. H. Zhang, Z. P. Hou, Electric field manipulation of magnetic skyrmions. *Rare Met.* **41**, 4000–4014 (2022).
6. H. Zhang, Y. Zhang, Z. Hou, M. Qin, X. Gao, J. Liu, Magnetic skyrmions: Materials, manipulation, detection, and applications in spintronic devices. *Mater. Futures* **2**, 032201 (2023).
7. Z. Hou, Q. Zhang, X. Zhang, G. Xu, J. Xia, B. Ding, H. Li, S. Zhang, N. M. Batra, P. M. F. J. Costa, E. Liu, G. Wu, M. Ezawa, X. Liu, Y. Zhou, X. Zhang, W. Wang, Current-induced helicity reversal of a single skyrmionic bubble chain in a nanostructured frustrated magnet. *Adv. Mater.* **32**, e1904815 (2020).
8. D. Yu, Y. Ga, J. Liang, C. Jia, H. Yang, Voltage-controlled Dzyaloshinskii-Moriya interaction torque switching of perpendicular magnetization. *Phys. Rev. Lett.* **130**, 056701 (2023).
9. C. Jin, Z.-A. Li, A. Kovács, J. Caron, F. Zheng, F. N. Rybakov, N. S. Kiselev, H. Du, S. Blügel, M. Tian, Y. Zhang, M. Farle, R. E. Dunin-Borkowski, Control of morphology and formation of highly geometrically confined magnetic skyrmions. *Nat. Commun.* **8**, 15569 (2017).
10. J. Tang, Y. Wu, W. Wang, L. Kong, B. Lv, W. Wei, J. Zang, M. Tian, H. Du, Magnetic skyrmion bundles and their current-driven dynamics. *Nat. Nanotechnol.* **16**, 1086–1091 (2021).
11. F. Zheng, N. S. Kiselev, F. N. Rybakov, L. Yang, W. Shi, S. Blügel, R. E. Dunin-Borkowski, Hopfion rings in a cubic chiral magnet. *Nature* **623**, 718–723 (2023).
12. Z. He, Z. Li, Z. Chen, Z. Wang, J. Shen, S. Wang, C. Song, T. Zhao, J. Cai, S.-Z. Lin, Y. Zhang, B. Shen, Experimental observation of current-driven antiskyrmion sliding in stripe domains. *Nat. Mater.* **23**, 1048–1054 (2024).
13. A. N. Bogdanov, U. K. Rößler, Chiral symmetry breaking in magnetic thin films and multilayers. *Phys. Rev. Lett.* **87**, 037203 (2001).

14. G. Yu, P. Upadhyaya, Q. Shao, H. Wu, G. Yin, X. Li, C. He, W. Jiang, X. Han, P. K. Amiri, K. L. Wang, Room-temperature skyrmion shift device for memory application. *Nano Lett.* **17**, 261–268 (2017).

15. J. Liu, Z. Wang, T. Xu, H. Zhou, H. Zhao, S.-G. Je, M.-Y. Im, L. Fang, W. Jiang, The 20-nm skyrmion generated at room temperature by spin-orbit torques. *Chinese Phys. Lett.* **39**, 017501 (2022).

16. W. Legrand, D. Maccariello, F. Ajejas, S. Collin, A. Vecchiola, K. Bouzehouane, N. Reyren, V. Cros, A. Fert, Room-temperature stabilization of antiferromagnetic skyrmions in synthetic antiferromagnets. *Nat. Mater.* **19**, 34–42 (2020).

17. B. He, H. Jin, D. Zheng, Y. Liu, J. Li, Y. Hu, Y. Wang, J. Zhang, Y. Peng, C. Wan, T. Zhu, X. Han, S. Zhang, G. Yu, Creation of room-temperature sub-100 nm antiferromagnetic skyrmions in an antiferromagnet IrMn through interfacial exchange coupling. *Nano Lett.* **24**, 2196–2202 (2024).

18. V. T. Pham, N. Sisodia, I. Di Manici, J. Urrestarazu-Larrañaga, K. Bairagi, J. Pelloux-Prayer, R. Guedas, L. D. Buda-Prejbeanu, A. Auffret, T. O. Menteş, S. Pizzini, P. Kumar, A. Finco, V. Jacques, G. Gaudin, O. Boulle, Fast current-induced skyrmion motion in synthetic antiferromagnets. *Science* **384**, 307–312 (2024).

19. S. Woo, K. Litzius, B. Krüger, M.-Y. Im, L. Caretta, K. Richter, M. Mann, A. Krone, R. M. Reeve, M. Weigand, P. Agrawal, I. Lemesh, M.-A. Mawass, P. Fischer, M. Kläui, G. S. D. Beach, Observation of room-temperature magnetic skyrmions and their current-driven dynamics in ultrathin metallic ferromagnets. *Nat. Mater.* **15**, 501–506 (2016).

20. O. Boulle, J. Vogel, H. Yang, S. Pizzini, D. De Souza Chaves, A. Locatelli, T. O. Menteş, A. Sala, L. D. Buda-Prejbeanu, O. Klein, M. Belmeguenai, Y. Roussigné, A. Stashkevich, S. M. Chérif, L. Aballe, M. Foerster, M. Chshiev, S. Auffret, I. M. Miron, G. Gaudin, Room-temperature chiral magnetic skyrmions in ultrathin magnetic nanostructures. *Nat. Nanotechnol.* **11**, 449–454 (2016).

21. A. Soumyanarayanan, M. Raju, A. L. Gonzalez Oyarce, A. K. C. Tan, M.-Y. Im, A. P. Petrović, P. Ho, K. H. Khoo, M. Tran, C. K. Gan, F. Ernult, C. Panagopoulos, Tunable room-temperature magnetic skyrmions in Ir/Fe/Co/Pt multilayers. *Nat. Mater.* **16**, 898–904 (2017).

22. Y. Wang, L. Wang, J. Xia, Z. Lai, G. Tian, X. Zhang, Z. Hou, X. Gao, W. Mi, C. Feng, M. Zeng, G. Zhou, G. Yu, G. Wu, Y. Zhou, W. Wang, X.-X. Zhang, J. Liu, Electric-field-driven non-volatile multi-state switching of individual skyrmions in a multiferroic heterostructure. *Nat. Commun.* **11**, 3577 (2020).

23. Z. Hou, Y. Wang, X. Lan, S. Li, X. Wan, F. Meng, Y. Hu, Z. Fan, C. Feng, M. Qin, M. Zeng, X. Zhang, S. Liu, X. Fu, G. Yu, G. Zhou, Y. Zhou, W. Zhao, X. Gao, J.-M. Liu, Controlled switching of the number of skyrmions in a magnetic nanodot by electric fields. *Adv. Mater.* **34**, e2107908 (2022).

24. Y. Sun, T. Lin, N. Lei, X. Chen, W. Kang, Z. Zhao, D. Wei, C. Chen, S. Pang, L. Hu, L. Yang, E. Dong, L. Zhao, L. Liu, Z. Yuan, A. Ullrich, C. H. Back, J. Zhang, D. Pan, J. Zhao, M. Feng, A. Fert, W. Zhao, Experimental demonstration of a skyrmion-enhanced strain-mediated physical reservoir computing system. *Nat. Commun.* **14**, 3434 (2023).

25. Y. Ba, S. Zhuang, Y. Zhang, Y. Wang, Y. Gao, H. Zhou, M. Chen, W. Sun, Q. Liu, G. Chai, J. Ma, Y. Zhang, H. Tian, H. Du, W. Jiang, C. Nan, J.-M. Hu, Y. Zhao, Electric-field control of skyrmions in multiferroic heterostructure via magnetoelectric coupling. *Nat. Commun.* **12**, 322 (2021).

26. R. Chen, C. Chen, L. Han, P. Liu, R. Su, W. Zhu, Y. Zhou, F. Pan, C. Song, Ordered creation and motion of skyrmions with surface acoustic wave. *Nat. Commun.* **14**, 4427 (2023).

27. Y. Yang, L. Zhao, D. Yi, T. Xu, Y. Chai, C. Zhang, D. Jiang, Y. Ji, D. Hou, W. Jiang, J. Tang, P. Yu, H. Wu, T. Nan, Acoustic-driven magnetic skyrmion motion. *Nat. Commun.* **15**, 1018 (2024).

28. K. Shibata, J. Iwasaki, N. Kanazawa, S. Aizawa, T. Tanigaki, M. Shirai, T. Nakajima, M. Kubota, M. Kawasaki, H. S. Park, D. Shindo, N. Nagaosa, Y. Tokura, Large anisotropic deformation of skyrmions in strained crystal. *Nat. Nanotechnol.* **10**, 589–592 (2015).

29. J.-M. Hu, T. Yang, L.-Q. Chen, Strain-mediated voltage-controlled switching of magnetic skyrmions in nanostructures. *npj Comput. Mater.* **4**, 62 (2018).

30. J. Wang, J. Zhang, A real-space phase field model for the domain evolution of ferromagnetic materials. *Int. J. Solids Struct.* **50**, 3597–3609 (2013).

31. A. Chacon, A. Bauer, T. Adams, F. Rucker, G. Brandl, R. Georgii, M. Garst, C. Pfleiderer, Uniaxial pressure dependence of magnetic order in MnSi. *Phys. Rev. Lett.* **115**, 267202 (2015).

32. A. S. Sukhanov, P. Vir, A. Heinemann, S. E. Nikitin, D. Kriegner, H. Borrmann, C. Shekhar, C. Felser, D. S. Inosov, Giant enhancement of the skyrmion stability in a chemically strained helimagnet. *Phys. Rev. B* **100**, 180403 (2019).

33. Y. Nii, T. Nakajima, A. Kikkawa, Y. Yamasaki, K. Ohishi, J. Suzuki, Y. Taguchi, T. Arima, Y. Tokura, Y. Iwasa, Uniaxial stress control of skyrmion phase. *Nat. Commun.* **6**, 8539 (2015).

34. Y. Shi, J. Wang, Stabilizing skyrmions by nonuniform strain in ferromagnetic thin films without a magnetic field. *Phys. Rev. B* **97**, 224428 (2018).

35. S. Seki, Y. Okamura, K. Shibata, R. Takagi, N. D. Khanh, F. Kagawa, T. Arima, Y. Tokura, Stabilization of magnetic skyrmions by uniaxial tensile strain. *Phys. Rev. B* **96**, 220404 (2017).

36. J. Wang, Mechanical control of magnetic order: From phase transition to skyrmions. *Annu. Rev. Mater. Res.* **49**, 361–388 (2019).

37. C. Liu, J. Wang, W. He, C. Zhang, S. Zhang, S. Yuan, Z. Hou, M. Qin, Y. Xu, X. Gao, Y. Peng, K. Liu, Z. Q. Qiu, J.-M. Liu, X. Zhang, Strain-induced reversible motion of skyrmions at room temperature. *ACS Nano* **18**, 761–769 (2024).

38. D. Kong, A. Kovács, M. Charilaou, F. Zheng, L. Wang, X. Han, R. E. Dunin-Borkowski, Direct observation of tensile-strain-induced nanoscale magnetic hardening. *Nat. Commun.* **14**, 3963 (2023).

39. L. Deng, H.-C. Wu, A. P. Litvinchuk, N. F. Q. Yuan, J.-J. Lee, R. Dahal, H. Berger, H.-D. Yang, C.-W. Chu, Room-temperature skyrmion phase in bulk Cu_2OSeO_3 under high pressures. *Proc. Natl. Acad. Sci. U.S.A.* **117**, 8783–8787 (2020).

40. Z. Mahimwalla, K. G. Yager, J.-I. Mamiya, A. Shishido, A. Priimagi, C. J. Barrett, Azobenzene photomechanics: Prospects and potential applications. *Polym. Bull.* **69**, 967–1006 (2012).

41. L. Wang, C. Liu, N. Mehmood, G. Han, Y. Wang, X. Xu, C. Feng, Z. Hou, Y. Peng, X. Gao, G. Yu, Construction of a room-temperature Pt/Co/Ta multilayer film with ultrahigh-density skyrmions for memory application. *ACS Appl. Mater. Interfaces* **11**, 12098–12104 (2019).

42. Z. Hou, Q. Wang, Q. Zhang, S. Zhang, C. Zhang, G. Zhou, X. Gao, G. Zhao, X. Zhang, W. Wang, J. Liu, Current-induced reversible split of elliptically distorted skyrmions in geometrically confined Fe_3Sn_2 nanotrack. *Adv. Sci.* **10**, 2206106 (2023).

43. S.-Z. Lin, Edge instability in a chiral stripe domain under an electric current and skyrmion generation. *Phys. Rev. B* **94**, 020402 (2016).

44. K. M. Song, J.-S. Jeong, B. Pan, X. Zhang, J. Xia, S. Cha, T.-E. Park, K. Kim, S. Finizio, J. Raabe, J. Chang, Y. Zhou, W. Zhao, W. Kang, H. Ju, S. Woo, Skyrmion-based artificial synapses for neuromorphic computing. *Nat. Electron.* **3**, 148–155 (2020).

45. K. Wang, Y. Zhang, V. Bheemarasetty, S. Zhou, S.-C. Ying, G. Xiao, Single skyrmion true random number generator using local dynamics and interaction between skyrmions. *Nat. Commun.* **13**, 722 (2022).

46. P.-J. Hsu, A. Kubetzka, A. Finco, N. Romming, K. Von Bergmann, R. Wiesendanger, Electric-field-driven switching of individual magnetic skyrmions. *Nat. Nanotechnol.* **12**, 123–126 (2017).

47. H. Du, R. Che, L. Kong, X. Zhao, C. Jin, C. Wang, J. Yang, W. Ning, R. Li, C. Jin, X. Chen, J. Zang, Y. Zhang, M. Tian, Edge-mediated skyrmion chain and its collective dynamics in a confined geometry. *Nat. Commun.* **6**, 8504 (2015).

48. B. Cui, D. Yu, Z. Shao, Y. Liu, H. Wu, P. Nan, Z. Zhu, C. Wu, T. Guo, P. Chen, H.-A. Zhou, L. Xi, W. Jiang, H. Wang, S. Liang, H. Du, K. L. Wang, W. Wang, K. Wu, X. Han, G. Zhang, H. Yang, G. Yu, Néel-type elliptical skyrmions in a laterally asymmetric magnetic multilayer. *Adv. Mater.* **33**, e2006924 (2021).

49. M. Schott, A. Bernand-Mantel, L. Ranno, S. Pizzini, J. Vogel, H. Béa, C. Baraduc, S. Auffret, G. Gaudin, D. Givord, The skyrmion switch: Turning magnetic skyrmion bubbles on and off with an electric field. *Nano Lett.* **17**, 3006–3012 (2017).

50. M. Heide, G. Bihlmayer, S. Blügel, Dzyaloshinskii-Moriya interaction accounting for the orientation of magnetic domains in ultrathin films: Fe/W(110). *Phys. Rev. B* **78**, 140403 (2008).

51. B. Dang, K. Liu, X. Wu, Z. Yang, L. Xu, Y. Yang, R. Huang, One-phototransistor–one-memristor array with high-linearity light-tunable weight for optic neuromorphic computing. *Adv. Mater.* **35**, e2204844 (2023).

52. T. Li, J. Miao, T. Fu, B. Song, B. Cai, X. Ge, X. Zhou, P. Zhou, X. Wang, D. Jariwala, W. Hu, Reconfigurable, non-volatile neuromorphic photovoltaics. *Nat. Nanotechnol.* **18**, 1303–1310 (2023).

53. K. Shahbazi, J.-V. Kim, H. T. Nembach, J. M. Shaw, A. Bischof, M. D. Rossell, V. Jeudy, T. A. Moore, C. H. Marrows, Domain-wall motion and interfacial Dzyaloshinskii-Moriya interactions in Pt/Co/Ir(Ir)/Ta multilayers. *Phys. Rev. B* **99**, 094409 (2019).

54. A. W. J. Wells, P. M. Shepley, C. H. Marrows, T. A. Moore, Effect of interfacial intermixing on the Dzyaloshinskii-Moriya interaction in Pt/Co/Pt. *Phys. Rev. B* **95**, 054428 (2017).

55. T. Balashov, T. Schuh, A. F. Takács, A. Ernst, S. Ostanin, J. Henk, I. Mertig, P. Bruno, T. Miyamachi, S. Suga, W. Wulfhekel, Magnetic anisotropy and magnetization dynamics of individual atoms and clusters of Fe and Co on Pt(111). *Phys. Rev. Lett.* **102**, 257203 (2009).

56. X. Liu, M. M. Steiner, R. Sooryakumar, G. A. Prinz, R. F. C. Farrow, G. Harp, Exchange stiffness, magnetization, and spin waves in cubic and hexagonal phases of cobalt. *Phys. Rev. B* **53**, 12166–12172 (1996).

57. X. Wan, Y. Hu, B. Wang, First and second order rotational transitions of skyrmion crystal in multiferroic Cu_2OSeO_3 under electric field. *App. Phys. Lett.* **116**, 182403 (2020).

58. X. Wan, Y. Hu, B. Wang, Exchange-anisotropy-induced intrinsic distortion, structural transition, and rotational transition in skyrmion crystals. *Phys. Rev. B* **98**, 174427 (2018).

Acknowledgments